Electret-based microgenerators under sinusoidal excitations: an analytical modeling

Cuong C. Nguyen[*1,2], Damith C. Ranasinghe[2a] and Said F. Al-Sarawi[1b]

[1]*Centre for Biomedical Engineering, School of Electrical and Electronic Engineering,
University of Adelaide, Adelaide, SA 5005, Australia*
[2]*Auto-ID Lab, School of Computer Science, University of Adelaide, Adelaide, SA 5005, Australia*

Abstract. The fast-growing number of mobile and wearable applications has driven several innovations in small-scale electret-based energy harvesting due to the compatibility with standard microfabrication processes and the ability to generate electrical energy from ambient vibrations. However, the current modeling methods used to design these small scale transducers or microgenerators are applicable only for constant-speed rotations and small sinusoidal translations, while in practice, large amplitude sinusoidal vibrations can happen. Therefore, in this paper, we formulate an analytical model for electret-based microgenerators under general sinusoidal excitations. The proposed model is validated using finite element modeling combined with numerical simulation approaches presented in the literature. The new model demonstrates a good agreement in estimating both the output voltage and power of the microgenerator. This new model provides useful insights into the microgenerator operating mechanism and design trade-offs, and therefore, can be utilized in the design and performance optimization of these small structures.

Keywords: energy harvesting; electrostatics; electret; vibration; microgenerator

1. Introduction

Extracting energy from ambient environment to power microelectronic devices is an emerging technology to achieve autonomous operation. Conventionally, energy can be harvested from four essential sources: light, radio frequency, thermal gradient and vibration due to motions (Bhatnagar *et al.* 2015). The practicability of each energy source varies and the choice to harvest which energy source mostly depends on the availability of the energy source in the applications. For mobile and wearable applications, vibration energy harvesting has been demonstrated to be the most promising technology and therefore, is attracting much interest.

Vibration energy harvesters convert mechanical vibrations to electrical energy by employing the three most common induction mechanisms: piezoelectric (Roundy *et al.* 2004, Yang *et al.* 2009, Wang *et al.* 2014), electromagnetic (Torah *et al.* 2008, Ju *et al.* 2013, Roundy *et al.* 2013) and electrostatic (Meninger *et al.* 2001, Yen *et al.* 2006, Kiziroglou *et al.* 2009). The utilization of each power transduction mechanism has its strengths and weaknesses and the decision to select a harvesting technology is mostly dependent on the applications. For miniaturization using micro-electro-mechanical-system (MEMS) fabrication processes, electrostatic based microgenerators with pre-charged electret provide a unique opportunity to produce a sufficient amount of energy to power wireless sensors or actuators used in the mobile or wearable applications (Jefimenko *et al.* 1978, Tada 1992, Boland *et al.* 2003, Lo *et al.* 2008, Yang *et al.* 2014, Perez *et al.* 2016).

In our previous work (Nguyen *et al.* 2017), we formulated an analytical model to describe the dynamic behavior of electret-based microgenerators under sinusoidal excitations with small excitation amplitudes, while in practice, large excitation amplitudes do also exist (Tsutsumino *et al.* 2006, Naruse *et al.* 2009, Chen *et al.* 2013). The effect of multiple electrode crossing has been numerically investigated in the literature, however, with little in-depth insight into the operation mechanism of such devices (Renaud *et al.* 2015). As a result, this opens an interesting opportunity to extend the initially developed model to take into consideration a general excitation amplitude and provide an accurate prediction of power and voltage generated by the microgenerator. Hence, in this paper, we generalize the model developed in (Nguyen *et al.* 2017) to highlight the addressed opportunity.

The paper is organized as follows: Sect. 2 presents the theoretical formulation to model the microgenerator using linear circuit elements. A practical model of the microgenerator, including the effect of parasitic capacitances, is then presented in Sect. 3. In Sect. 4, the proposed model is validated by comparing it with numerically simulated results presented in the literature (Boisseau *et al.* 2010) and followed by a conclusion and an acknowledgment.

∗Corresponding author, Master Student
 E-mail: cuong.nguyen@adelaide.edu.au
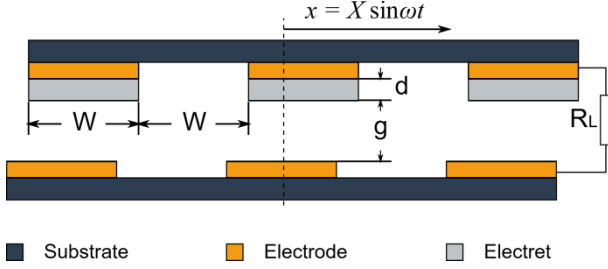[a] Ph.D.
[b] Ph.D.

Substabte | Electrode | Electret

Fig. 1 Schematic of an electret-based cross-wafer microgenerator

2. Theoretical model

The electret-based microgenerator considered in this paper is a non-parametric structure in which the electrode width equals to the gap spacing between the two electrodes as illustrated in Fig. 1. The governing equation of the microgenerator which correlates the relative movement of the counter electrodes to the charge induced was derived by (Boland *et al.* 2003) as

$$\frac{dQ(t)}{dt} = -\left[\frac{Q(t)}{R_L C_0}\frac{A_0}{A(t)} + \frac{V_0}{R_L}\right] \tag{1}$$

where C_0 is the capacitance at 100 percent overlapping area A_0, and V_0 is the surface potential of the electret. The capacitance C_0 can be calculated as

$$\frac{1}{C_0} = \frac{d}{\varepsilon_d \varepsilon_0 A_0} + \frac{g}{\varepsilon_0 A_0} \Rightarrow C_0 = \frac{\varepsilon_d \varepsilon_0 A_0}{d + \varepsilon_d g} \tag{2}$$

where ε_d is the dielectric constant of electret, ε_0 is the permittivity of freespace, d and g are electret thickness and gap spacing between the two plates of the microgenerator, respectively.

Eq. (1) shows a dependency of the induced charge $Q(t)$ on the instantaneous overlapping area $A(t)$, which is directly related to the type of external excitations. Therefore, to investigate the performance of the electret-based microgenerator, it is essential to determine the correlation between the excitation $x(t)$ and instantaneous overlapping area $A(t)$. For the simplest case, which is a constant-speed rotation, the overlapping area is directly proportional to time and therefore, the solution of Eq. (1) can be easily obtained (Boland *et al.* 2003). For sinusoidal translations $x(t) = X \sin \omega t$, the correlation between $A(t)$ and $x(t)$ is a triangle wave as shown in Fig. 2 which can be formulated as

$$A(t) = \frac{2A_0}{\pi}\left|\arcsin\left\{\sin\left[\frac{\pi x(t)}{2W}\right]\right\}\right| \tag{3}$$

where W is the electrode width of the electret-based microgenerator.

The absolute function included in Eq. (3) is to represent both the symmetry of the excitation and the non-negativity of instantaneous overlapping area $A(t)$. To investigate the performance of the electret-based microgenerator for a general value of the vibration amplitude X to the electrode width W - defined as k, a similar approach to the one

considered in (Nguyen *et al.* 2017) is employed. The assumptions of periodic nature of the excitation and symmetry of the microgenerator are utilized, so that only a first half cycle of the excitation is analyzed. Within this time period, Eq. (3) can be represented using a piecewise function

$$\frac{A(t)}{A_0} = \begin{cases} \frac{x(t)}{W} - 2m, & 2m < \frac{x(t)}{W} \leq 2m + 1 \\ 2m + 2 - \frac{x(t)}{W}, & 2m + 1 < \frac{x(t)}{W} \leq 2m + 2, \end{cases} \tag{4}$$

where m is a natural number within $[0, k/2)$ and $k = X/W$ is the ratio between the excitation amplitude and the electrode width.

For example, when $k \in (0, 1]$, which corresponds to the small amplitude excitation case, only one value of $m = 0$ is satisfied and the overlapping area can be expressed as

$$\frac{A(t)}{A_0} = \frac{x(t)}{W} = k \sin \omega t \tag{5}$$

which is consistent with the result in (Nguyen *et al.* 2017). It is important to note that the expression in (5) is not associated with an absolute operator as the one presented in (Nguyen *et al.* 2017) due to the assumption which considers only a first half cycle of the vibration. When $k \in (1, 2]$, there is also one value of $m = 0$, but the overlapping area is a combination of two sub-functions given by

$$\frac{A(t)}{A_0} = \begin{cases} k \sin \omega t, & 0 < \frac{x(t)}{W} \leq 1 \\ 2 - k \sin \omega t, & 1 < \frac{x(t)}{W} \leq 2 \end{cases} \tag{6}$$

Table 1 provides a list of values of m and the number of sub-functions used to describe $A(t)$ under different values of k. In general, the shape of the overlapping area, in the time domain, is analogous to a sinusoidal function that is folded $(k - 1)$ times between 0 and 1 as illustrated in Fig. 3. As a result, $A(t)$ is a combination of $(2k - 1)$ sub-functions.

For simplicity, the following analysis is carried out with integer values of k. Nonetheless, a non-integer k can also be analyzed by replacing the value k only in the superscript index notation presented in the following by the ceiling value of k, while all the calculations relate to k are unchanged.
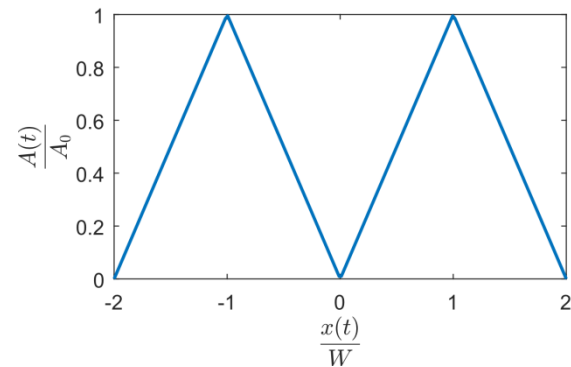

Fig. 2 Instantaneous overlapping area $A(t)$ is a triangle wave with respect to the displacement $x(t)$
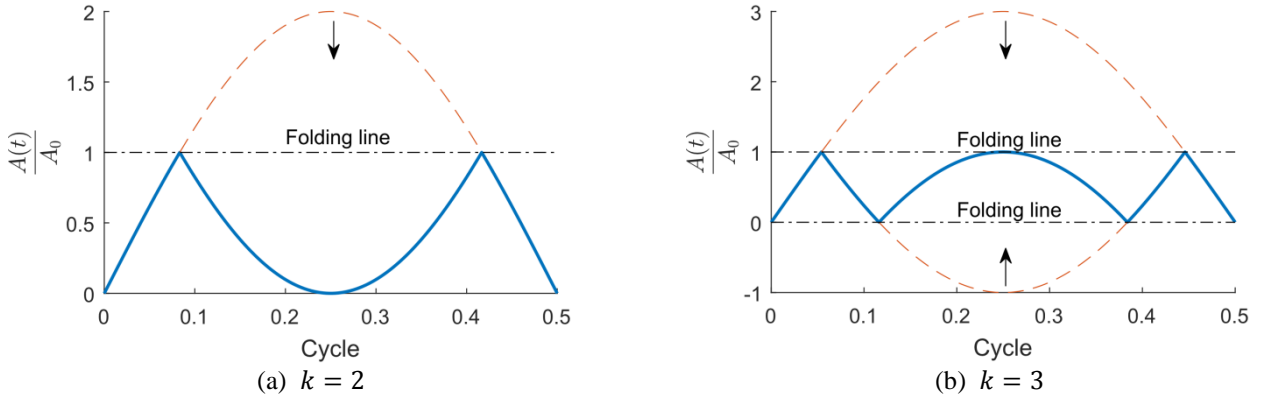
(a) $k = 2$

(b) $k = 3$

Fig. 3 Instantaneous overlapping area is represented by a piecewise function which is analogous to a sinusoidal function folded into $(k - 1)$ segments between 0 and 1 in the y-axis

Table 1 Example of range of m and the number of segments expressed the overlapping area $A(t)$ with different values of k

k	m	Number of sub-functions
1	0	1
2	0	2
3	0, 1	3
4	0, 1	4
5	0, 1, 2	5

The expression of $A(t)$ given in Eq. (4) is substituted into Eq. (1) to solve for the induced charge $Q(t)$. However, the non-linearity of the sinusoidal function associated in the overlapping area $A(t)$ complicates the solution and places a roadblock for a further analysis. To reduce the non-linearity and ease the analysis, one common approach is to approximate the sinusoidal function using a polynomial. The higher the order of the polynomial used, the more accurate the approximation. However, a too high order polynomial also accompanies a sophisticated solution and consequently, undesirable. As shown in Fig. 4 within the first half cycle of the excitation, a sinusoidal function can be approximated using a second order polynomial, also known as a parabolic function presented as

$$\sin \omega t \approx \frac{4\omega t}{\pi}\left(1 - \frac{\omega t}{\pi}\right) \qquad (7)$$

Hence, Eq. (4) can be rewritten by replacing $x(t)$ by the parabolic function given in (7). The interval defining each sub-function of the piecewise function presented in Eq. (4) is also rewritten by solving the corresponding inequalities given in Eq. (4) and expressed in term of time instance t_j. The resulting overlapping area $A(t)$ is then given by

$$\frac{A(t)}{A_0}$$
$$= \begin{cases} 4k\frac{\omega t}{\pi}\left(1 - \frac{\omega t}{\pi}\right) - 2m, & t_{2m} \leq t < t_{2m+1} \ or \ t_{2k-2m} \leq t < t_{2k+1-2m} \\ 2m + 2 - 4k\frac{\omega t}{\pi}\left(1 - \frac{\omega t}{\pi}\right), & t_{2m+1} \leq t < t_{2m+2} \ or \ t_{2k-2m-1} \leq t < t_{2k-2m}, \end{cases} \qquad (8)$$

where

$$t_j = \begin{cases} \tau_j, & 0 \leq j \leq k \\ \frac{\pi}{\omega} - \tau_{2k+1-j}, & k + 1 \leq j \leq 2k + 1 \end{cases} \qquad (9)$$

and τ_j is defined as

$$\tau_j = \left(1 - \sqrt{1 - \frac{j}{k}}\right)\frac{\pi}{2\omega} \qquad (10)$$

Here, t_j can also be understood as the time instance that satisfies $A(t_j) = 0$ or $A(t_j) = A_0$. The purpose of using the notation τ_j is to simplify the representation of the time instance t_j. Within each time interval $[t_j, t_{j+1}]$, $A(t)$ can be presented by one continuous sub-function. However, with such definition of the time instance t_j given in Eq. (9), there is a special case in which

$$t_k = t_{k+1} = \frac{\pi}{2\omega} \qquad (11)$$

This corresponds to the time instance at the middle cycle of the excitation and the duration of the time interval $[t_k, t_{k+1}]$ is, therefore, zero. As a result, the two time instances t_k and t_{k+1} are excluded from the following analysis. Thus, all of the notation indexes discussed later also exclude the two values k and $(k + 1)$.

The dynamic behavior of the microgenerator within each time interval as part of the overlapping area given in Eq. (8) is analyzed in the following sub-sections.

2.1 Time interval $t_{2m} \leq t < t_{2m+1}$ or $t_{2k-2m} \leq t < t_{2k+1-2m}$

Within this time interval, the overlapping area is defined according to Eq. (8). Eq. (1) can, therefore, be written as

$$\frac{dQ_1(t)}{dt} = -\left\{\frac{Q_1(t)}{kR_LC_0\left[\frac{4\omega t}{\pi}\left(1 - \frac{\omega t}{\pi}\right) - \frac{2m}{k}\right]} + \frac{V_0}{R_L}\right\} \qquad (12)$$
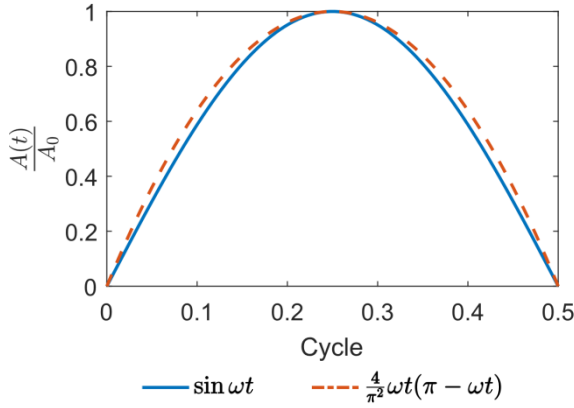
Fig. 4 Within a first half cycle of the excitation, a sinusoidal function can be approximated using a parabolic function

The induced charge $Q_1(t)$ can be solved by employing integrating factor method combined with the result 3.194-1 in (Gradshteyn *et al.* 2014) and the Euler's transform of hypergeometric functions in the result (5.5) in (Temme 2011). Further details of the solution are included in Appx. A. The solution of Eq. (12) can then be expressed as

$$Q_1(t) = \beta_1 \left(\frac{t_{2k+1-2m} - t}{t - t_{2m}} \right)^{\gamma_{2m}}$$
$$- \frac{V_0(t - t_{2m})(t_{2k+1-2m} - t)}{R_L(1 + \gamma_{2m})(t_{2k+1-2m} - t_{2m})} \quad (13)$$
$$\times {}_2F_1 \left(1, 2; 2 + \gamma_{2m}; \frac{t - t_{2m}}{t_{2k+1-2m} - t_{2m}} \right)$$

where β_1 is an arbitrary constant, ${}_2F_1(a, b; c; z)$ is a hypergeometric function, and

$$\gamma_j = \frac{\pi}{4k\omega R_L C_0 \sqrt{1 - \frac{j}{k}}} \quad (14)$$

At time $t = t_{2m}$, there is no overlap between the two plates of the electret-based microgenerator and therefore, no charge is induced or $Q_1(t_{2m}) = 0$. This results in $\beta_1 = 0$ and a simpler solution is obtained. In spite of that, the non-linearity of the hypergeometric function in Eq. (13) is quite complicated and consequently, does not allow modeling the microgenerator using linear circuit elements. Therefore, we employ the series expansion of hypergeometric functions to linearize the solution for further analysis. By expanding the hypergeometric function in Eq. (13), the solution of charge $Q_1(t)$ can be written as

$$Q_1(t) = - \frac{V_0(t - t_{2m})(t_{2k+1-2m} - t)}{R_L(1 + \gamma_{2m})(t_{2k+1-2m} - t_{2m})}$$
$$\times {}_2F_1 \left(1, 2; 2 + \gamma_{2m}; \frac{t - t_{2m}}{t_{2k+1-2m} - t_{2m}} \right)$$
$$= - \frac{V_0(t - t_{2m})(t_{2k+1-2m} - t)}{R_L(1 + \gamma_{2m})(t_{2k+1-2m} - t_{2m})} \quad (15)$$
$$\times \left(1 + \frac{2}{2 + \gamma_{2m}} \frac{t - t_{2m}}{t_{2k+1-2m} - t_{2m}} + \cdots \right)$$

Owing to the microscale of the microgenerator, the system capacitance C_0 is small and often less than 10 pF. The external load R_L can vary from a few kΩ to a few hundred MΩ. In addition, the targeted vibration frequency, from the application point of view, is very low, which is in the order of 2 Hz for human motion (Yun *et al.* 2011). As a result, $\omega R_L C_0$ is very small, making the lowest order term in the series expansion become the dominant term. We can, therefore, approximate the hypergeometric function to the lowest order term to obtain a closed-form solution of induced charge $Q_1(t)$ as

$$Q_1(t) = - \frac{V_0(t - t_{2m})(t_{2k+1-2m} - t)}{R_L(1 + \gamma_{2m})(t_{2k+1-2m} - t_{2m})} \quad (16)$$

Given the induced charge in Eq. (16), the electric current passing through the external load and the output voltage can respectively be calculated as

$$I_1(t) = - \frac{dQ_1(t)}{dt}$$
$$= \frac{\pi V_0 \left(1 - \frac{2\omega t}{\pi} \right)}{\omega R_L(1 + \gamma_{2m})(t_{2k+1-2m} - t_{2m})} \quad (17)$$

$$V_1(t) = R_L I_1(t) = \frac{\pi V_0 \left(1 - \frac{2\omega t}{\pi} \right)}{\omega(1 + \gamma_{2m})(t_{2k+1-2m} - t_{2m})} \quad (18)$$

We then investigate the two important characteristics of the microgenerator: short circuit current and open circuit voltage in order to utilize linear circuit elements to model the microgenerator. The short circuit current can be determined as the external load is set to zero, while the open circuit voltage is obtained when the load approaches infinity

$$I_{sc_1}(t) = \lim_{R_L \to 0} I_1(t) = \frac{4k\omega C_0 V_0}{\pi} \left(1 - \frac{2\omega t}{\pi} \right) \quad (19)$$

$$V_{oc_1}(t) = \lim_{R_L \to \infty} V_1(t) = \frac{V_0}{\sqrt{1 - \frac{2m}{k}}} \left(1 - \frac{2\omega t}{\pi} \right) \quad (20)$$

The results in (19) and (20) show that the short circuit current is directly proportional to the open circuit voltage, which represents the characteristic of a resistor. The microgenerator can, therefore, be modeled as a reverse-sawtooth voltage source $V_{sc_1}(t)$ in series with an equivalent internal resistance R_{i_1} defined as

$$R_{i_1} = \frac{V_{oc_1}(t)}{I_{sc_1}(t)} = \frac{\pi}{4k\omega C_0 \sqrt{1 - \frac{2m}{k}}} = \frac{R_0}{8k \sqrt{1 - \frac{2m}{k}}} \quad (21)$$

where $R_0 = 1/(fC_0)$.

Remark 1. R_0 is a direct analogy to the equivalent resistance of a switch capacitor C_0 at a switching frequency f as presented in (Franco 2002: 187-88). Therefore, the dynamic behavior of the electret-based microgenerator in this case is analogous to the operation mechanism of a switch capacitor.
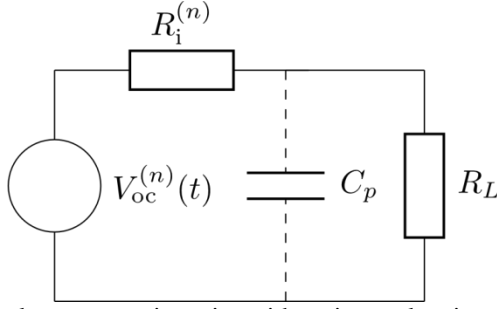
(a) A voltage source in series with an internal resistance
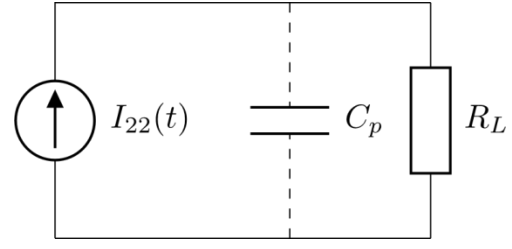
(b) A current source

Fig. 5 The electret-based microgenerator under a sinusoidal excitation with angular frequency ω can be modeled using linear circuit elements. Lumped parasitic capacitance is added to refine the model for accurate predictions
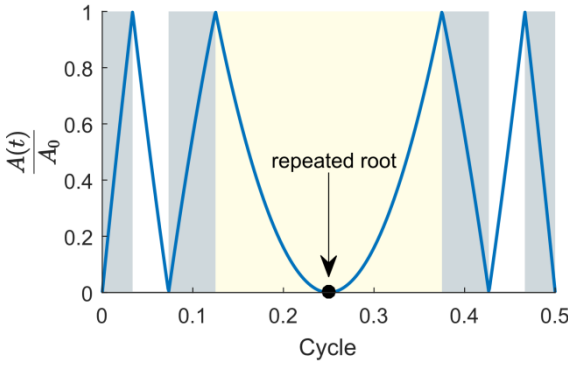

Fig. 6 Illustration of different time intervals corresponding to different electrodynamic responses of the electret-based microgenerator

The equivalent circuit of the electret-based microgenerator is presented in Fig. 5(a). In addition, for the case of small amplitude excitations or $k \leq 1$, m can only equal to 0, the open circuit voltage and the equivalent internal resistance reduce to

$$\begin{cases} V_{oc_1}(t) = V_0 \left(1 - \dfrac{2\omega t}{\pi}\right) \\ R_{i_1} = \dfrac{R_0}{8k}, \end{cases} \tag{22}$$

which is consistent with the results formulated in (Nguyen *et al.* 2017).

2.2 Time interval $t_{2m+1} \leq t < t_{2m+2}$ or $t_{2k-2m-1} \leq t < t_{2k-2m}$

There is also a special case in the second branch of Eq. (8), which occurs when the ratio k is an even number. In this case, the overlapping area has a repeated time instances t_k and t_{k+1}, which is illustrated in Fig. 6. As stated in the paragraph right after Eq. (11), these two time instances are excluded and the time interval considered will be $[t_{k-1}, t_{k+2}]$. In addition to these repeated time instances when k is an even number, the integration in the time interval $[t_{k-1}, t_{k+2}]$ illustrated as the yellow-shaded region in Fig. 6 is different and therefore, is presented separately. In the following sections, the term "special case"

indicates the time interval $[t_{k-1}, t_{k+2}]$ when k is even, while the "general case" will cover the rest.

2.2.1 General case

The overlapping area in this case corresponds to the non-highlighted regions shown in Fig. 6. Within this time interval, the overlapping area is defined according to Eq. (8) and hence, Eq. (1) can be rewritten as

$$\frac{dQ_{21}(t)}{dt} = -\left\{ \frac{Q_{21}(t)}{kR_L C_0 \left[\frac{2m+2}{k} - \frac{4\omega t}{\pi}\left(1 - \frac{\omega t}{\pi}\right)\right]} + \frac{V_0}{R_L} \right\} \tag{23}$$

Eq. (23) can be solved using integrating factor method and the solution can be expressed as

$$\begin{aligned} Q_{21}(t) &= \beta_{21} \left(\frac{t - t_{2m+2}}{t - t_{2k-2m-1}}\right)^{\gamma_{2m+2}} \\ &\quad - \frac{V_0(t - t_{2m+2})(t - t_{2k-2m-1})}{R_L(1 + \gamma_{2m+2})(t_{2k-2m-1} - t_{2m+2})} \\ &\quad \times {}_2F_1\left(1, 2; 2 + \gamma_{2m+2}; \frac{t - t_{2k-2m-1}}{t_{2m+2} - t_{2k-2m-1}}\right) \end{aligned} \tag{24}$$

The details of solving Eq. (23) can be found in Appx. B.

At time $t = t_{2k-2m-1}$, there is no area overlap, resulting in no charge induced and therefore, $\beta_{21} = 0$. Similar to the approach presented in Sect. 2.1, the hypergeometric function in Eq. (24) is approximated to the lowest order term for the given reasons to obtain the closed-form solution as

$$Q_{21}(t) = -\frac{V_0(t - t_{2m+2})(t - t_{2k-2m-1})}{R_L(1 + \gamma_{2m+2})(t_{2k-2m-1} - t_{2m+2})} \tag{25}$$

Given the closed-form solution of the induced charge $Q_{21}(t)$ in Eq. (25), the output current and voltage are respectively calculated as

$$\begin{aligned} I_{21}(t) &= -\frac{dQ_{21}(t)}{dt} \\ &= \frac{-\pi V_0 \left(1 - \frac{2\omega t}{\pi}\right)}{\omega R_L(1 + \gamma_{2m+2})(t_{2k-2m-1} - t_{2m+2})} \end{aligned} \tag{26}$$

$$\begin{aligned} V_{21}(t) &= R_L I_{21}(t) \\ &= \frac{-\pi V_0 \left(1 - \frac{2\omega t}{\pi}\right)}{\omega(1 + \gamma_{2m+2})(t_{2k-2m-1} - t_{2m+2})} \end{aligned} \tag{27}$$

The short circuit current and open circuit voltage of the electret-based microgenerator in this case can be written respectively as

$$I_{sc_{21}}(t) = \lim_{R_L \to 0} I_{21}(t) = -\frac{4k\omega C_0 V_0}{\pi}\left(1 - \frac{2\omega t}{\pi}\right) \quad (28)$$

$$V_{oc_{21}}(t) = \lim_{R_L \to \infty} V_{21}(t) = \frac{-V_0}{\sqrt{1 - \frac{2m+2}{k}}}\left(1 - \frac{2\omega t}{\pi}\right) \quad (29)$$

Similar to the result obtained in Sect. 2.1, the short circuit current given in (28) is directly proportional to the open circuit voltage given in (29) which is, again, the characteristic of a resistor. Hence, the microgenerator can be modeled as a sawtooth voltage source $V_{oc_{21}}(t)$ in series with an equivalent internal resistance R_{i_2} illustrated in Fig. 5(a), where

$$R_{i_2} = \frac{R_0}{8k\sqrt{1 - \frac{2m+2}{k}}}. \quad (30)$$

To employ index-based notations to ease the further analysis, the internal resistances given in Eqs. (21) and (30) can be written as

$$R_i^{(n)} = \begin{cases} \dfrac{R_0}{8k\sqrt{1 - \dfrac{n + (n \bmod 2)}{k}}}, & 0 \le n \le k-1 \\[4mm] \dfrac{R_0}{8k\sqrt{1 - \dfrac{(2k-n) + [(2k-n) \bmod 2]}{k}}}, & k+2 \le n \le 2k \end{cases} \quad (31)$$

where mod is the modulo operator and the superscript (n) indicates that the variables are applicable in the time interval $[t_n,\ t_{n+1}]$ as illustrated in Fig. 7. Here, the values k and $(k+1)$ are excluded from the superscript index (n). The voltage sources specified in (20) and (29) can be rewritten in a single form as

$$V_{oc}^{(n)}(t) = (-1)^n \frac{8kR_i^{(n)}}{R_0} V_0 \left(1 - \frac{2\omega t}{\pi}\right) \quad (32)$$

2.2.2 Special case

In this case, k is an even number and therefore, there is a value of m such that $k = 2m + 2$, resulting in a repeated or double time instance that causes the overlapping area to be zero, illustrated as the yellow-shaded region shown in Fig. 6. The time interval considered for this case is presented as

$$t_{k-1} \le t \le t_{k+2}$$

Eq. (1) is, therefore, simplified to

$$\frac{dQ_{22}(t)}{dt} = -\left[\frac{Q_{22}(t)}{kR_LC_0\left(1 - \frac{2\omega t}{\pi}\right)^2} + \frac{V_0}{R_L}\right] \quad (33)$$

Appx. C presents the detailed formulation of the solution of Eq. (33). The solution of induced charge $Q_{22}(t)$ can be expressed as

$$Q_{22}(t) = \beta_{22} e^{\frac{-\pi}{2k\omega R_L C_0\left(1 - \frac{2\omega t}{\pi}\right)}} + \frac{\pi V_0}{2\omega R_L}\left(1 - \frac{2\omega t}{\pi}\right)$$
$$- \frac{V_0}{R_L}\frac{\pi^2 e^{\frac{-\pi}{2k\omega R_L C_0\left(1 - \frac{2\omega t}{\pi}\right)}}}{4k\omega^2 R_L C_0}$$
$$\times \text{Ei}\left[\frac{\pi}{2k\omega R_L C_0\left(1 - \frac{2\omega t}{\pi}\right)}\right] \quad (34)$$

where β_{22} is an arbitrary constant and $\text{Ei}(z)$ is the exponential integral function.

Owing to the continuity of the overlapping area in this time interval, the induced charge $Q_{22}(t)$ is also continuous. This continuity requires the equality of the left-handed limit to the right-handed limit, which can be expressed as

$$\lim_{t \to \left(\frac{\pi}{2\omega}\right)^-} Q_{22}(t) = \lim_{t \to \left(\frac{\pi}{2\omega}\right)^+} Q_{22}(t) \quad (35)$$

As a result of this continuity condition, $\beta_{22} = 0$.

We also employ the assumption of very small $\omega R_L C_0$ combined with the asymptotic representation of exponential integral function presented in the result 8.215 (Gradshteyn *et al.* 2014) to present the solution of induced charge $Q_{22}(t)$ as

$$Q_{22}(t) = \frac{\pi V_0}{2\omega R_L}\left(1 - \frac{2\omega t}{\pi}\right) - \frac{V_0}{R_L}\frac{\pi^2 e^{\frac{-\pi}{2k\omega R_L C_0\left(1 - \frac{2\omega t}{\pi}\right)}}}{4k\omega^2 R_L C_0}$$
$$\times \frac{2k\omega R_L C_0\left(1 - \frac{2\omega t}{\pi}\right)}{\pi}$$
$$\times \left\{1 + \frac{2k\omega R_L C_0\left(1 - \frac{2\omega t}{\pi}\right)}{\pi} + \cdots\right\}$$
$$\approx -2kC_0 V_0\left(1 - \frac{2\omega t}{\pi}\right)^2 \quad (36)$$

Given the linearized solution in (36), we can calculate the electrical current passing through the external load R_L as

$$I_{22}(t) = -\frac{dQ_{22}(t)}{dt} = -\frac{4k\omega C_0 V_0}{\pi}\left(1 - \frac{2\omega t}{\pi}\right) \quad (37)$$

The result in (37) shows that the output current is independent of the load resistance R_L, which is the characteristic of a current source. Therefore, the microgenerator, in this case, can be modeled as a current source $I_{22}(t)$ as shown in Fig. 5(b).

In summary, an electret-based microgenerator excited by a sinusoidal vibration can be modeled as a voltage source in series with an internal resistance as shown in Fig. 5(a). There is only one special case when k is an even number, the microgenerator can be modeled as a pure current source within the time interval $[t_{k-1},\ t_{k+2}]$ as shown in Fig. 5(b).

3. Effect of parasitic capacitances

The theoretical model developed in Sect. 2 neglects the effect of parasitic capacitances due to the harvesting circuit wiring and fringe capacitance within the microgenerator itself. Those unavoidable capacitances result in reducing the amount of energy transferred to the load. Consequently, the performance of the microgenerator is reduced, resulting in a notable discrepancy between the theoretical model prediction and measured data (Bartsch *et al.* 2009). To accurately predict the performance of the electret-based microgenerator, parasitic capacitances are lumped into a single capacitance C_p connected in parallel with the external load, R_L, as shown in Fig. 5. The governing equation of the circuit including C_p as shown in Fig. 5(a) is given by

$$C_p \frac{dV_{R_L}^{(n)}(t)}{dt} = \frac{V_{R_L}^{(n)}(t)}{R_p^{(n)}} - \frac{V_{oc}^{(n)}(t)}{R_L} \tag{38}$$

where $R_p^{(n)} = R_L || R_i^{(n)}$.

The solution of Eq. (38) can be expressed by

$$V_{R_L}^{(n)}(t) = c^{(n)} e^{\frac{-t}{R_p^{(n)} C_p}} + \phi^{(n)}(t) \tag{39}$$

where $c^{(n)}$ is an arbitrary constant, and $\phi^{(n)}(t)$ is the steady state response defined as

$$\phi^{(n)}(t) = \frac{(-1)^n 8 k R_p^{(n)} V_0}{R_0}\left(1 - \frac{2\omega t}{\pi} + \frac{2\omega R_p^{(n)} C_p}{\pi}\right) \tag{40}$$

For the special time interval $[t_{k-1}, t_{k+2}]$ when k is even, the microgenerator is equivalent to the circuit shown in Fig. 5(b) in which the governing equation is given by

$$C_p \frac{dV_{R_L}^{(k-1)}(t)}{dt} + \frac{V_{R_L}^{(k-1)}(t)}{R_L} = I_{22}(t) \tag{41}$$

The solution of Eq. (41) can be presented as

$$V_{R_L}^{(k-1)}(t) = c^{(k-1)} e^{\frac{-t}{R_L C_p}} + \psi(t) \tag{42}$$

where

$$\psi(t) = -\frac{4 k \omega R_L C_0 V_0}{\pi}\left(1 - \frac{2\omega t}{\pi} + \frac{2\omega R_L C_p}{\pi}\right) \tag{43}$$

To obtain a complete solution that includes the effect of parasitic capacitance C_p, the constants $c^{(n)}$ in Eq. (39) and $c^{(k-1)}$ in Eq. (42) must be determined by applying the condition of continuity of the output voltage $V_{R_L}^{(n)}(t)$ which means that $V_{R_L}^{(n)}(t_{n+1})$, the voltage at the end of the current time interval $[t_n, t_{n+1}]$, must equal to $V_{R_L}^{(n+1)}(t_{n+1})$, the voltage at the beginning of the next time interval $[t_{n+1}, t_{n+2}]$. In addition, the voltage at the end of the output cycle must be the same as the voltage at the beginning of the output cycle. These conditions can be mathematically presented as

$$\begin{cases} V_{R_L}^{(n)}(t_{n+1}) = V_{R_L}^{(n+1)}(t_{n+1}), & \text{when } 0 \le n \le 2k-1 \\ V_{R_L}^{(0)}(0) = V_{R_L}^{(2k)}\left(\frac{\pi}{\omega}\right) \end{cases} \tag{44}$$

Eq. (44) results in a system of $(2k-1)$ linear equations in term of $c^{(n)}$ and can be presented as

$$Ac = b \tag{45}$$

where A is a $(2k-1)$-by-$(2k-1)$ matrix, c is a vector containing $(2k-1)$ constants $c^{(n)}$, and b is a $(2k-1)$-dimensional vector.

For a general case without the repeated time instances causing zero overlapping area, the matrix A is given in Eq. (46). Each row of matrix A has only two non-zero elements, one is on the diagonal and one is next to the right of the diagonal. The last row is different, in which one element is still on the diagonal, while the other is in the first column. Here, it is important to note that the superscript indexes k and $(k+1)$ are excluded. That means the k-th row has two elements with their respective superscript indexes are $(k-1)$ and $(k+2)$.

$$A = \begin{pmatrix} e^{\frac{-t_1}{R_p^{(0)} C_p}} & -e^{\frac{-t_1}{R_p^{(1)} C_p}} & 0 & \cdots & 0 \\ 0 & e^{\frac{-t_2}{R_p^{(1)} C_p}} & -e^{\frac{-t_2}{R_p^{(2)} C_p}} & \cdots & 0 \\ \vdots & \vdots & \ddots & & \vdots \\ 0 & 0 & \cdots & e^{\frac{-t_{2k}}{R_p^{(2k-1)} C_p}} & -e^{\frac{-t_{2k}}{R_p^{(2k)} C_p}} \\ -e^{\frac{-t_0}{R_p^{(0)} C_p}} & 0 & \cdots & 0 & e^{\frac{-t_{2k+1}}{R_p^{(2k)} C_p}} \end{pmatrix} \tag{46}$$

The general form of vector b is presented in Eq. (47). Similar to matrix A, the element on the k-th row of vector b is the subtraction of two terms with their indexes as $(k+2)$ and $(k-1)$.

$$b = \begin{pmatrix} \phi^{(1)}(t_1) - \phi^{(0)}(t_1) \\ \phi^{(2)}(t_2) - \phi^{(1)}(t_2) \\ \vdots \\ \phi^{(2k)}(t_{2k}) - \phi^{(2k-1)}(t_{2k}) \\ \phi^{(0)}(t_0) - \phi^{(2k)}(t_{2k+1}) \end{pmatrix} \tag{47}$$

For the special case where the ratio k is an even number, the representation of the matrix A and vector b are slightly different from the general case given in Eqs. (46) and (47). The only modification needed is in $(k-1)$-th and k-th rows as highlighted in (48) and (49), while the rest is unchanged.

$$A = \begin{pmatrix} \cdots & e^{\frac{-t_{k-1}}{R_p^{(k-2)} C_p}} & -e^{\frac{-t_{k-1}}{R_p^{(k-1)} C_p}} & 0 & \cdots \\ \cdots & 0 & e^{\frac{-t_{k+2}}{R_p^{(k-1)} C_p}} & -e^{\frac{-t_{k+2}}{R_p^{(k+2)} C_p}} & \cdots \end{pmatrix}$$
$$\downarrow$$
$$A = \begin{pmatrix} \cdots & e^{\frac{-t_{k-1}}{R_p^{(k-2)} C_p}} & -e^{\frac{-t_{k-1}}{R_L C_p}} & 0 & \cdots \\ \cdots & 0 & e^{\frac{-t_{k+2}}{R_L C_p}} & -e^{\frac{-t_{k+2}}{R_p^{(k+2)} C_p}} & \cdots \end{pmatrix} \tag{48}$$

$$b = \begin{pmatrix} \vdots \\ \phi^{(k-1)}(t_{k-1}) - \phi^{(k-2)}(t_{k-1}) \\ \phi^{(k+2)}(t_{k+2}) - \phi^{(k-1)}(t_{k+2}) \\ \vdots \end{pmatrix}$$
$$\downarrow$$
$$b = \begin{pmatrix} \vdots \\ \psi(t_{k-1}) - \phi^{(k-2)}(t_{k-1}) \\ \phi^{(k+2)}(t_{k+2}) - \psi(t_{k+2}) \\ \vdots \end{pmatrix} \tag{49}$$
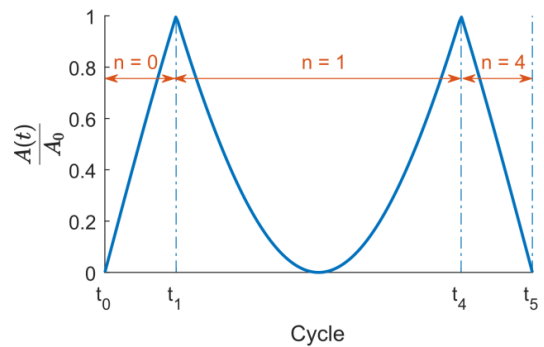

Fig. 7 An illustration of the superscript n corresponding to the time interval $[t_n, t_{n+1}]$ when $k = 2$. The indices k and $(k+1)$ are excluded from the analysis

Table 2 Parameters of the device presented in (Tsutsumino *et al.* 2006) are used to validate the analytical model

Parameter	Value
A_0	100 mm^2
W	0.5 mm
ε_d	2.1
V_0	-100 V
d	20 µm
g	100 µm, 175 µm and 200 µm
f	20 Hz
X	1 mm and 1.5 mm

Table 3 Lumped capacitances used in the analytical calculation and FEM capacitances used in the numerical simulation under different air gap distances and k, units are in µm for air gap g and pF for capacitances.

g	$C_{\min}$	$C_{\max}$	C_p	
			$k = 2$	$k = 3$
100	1.92	8.58	3.00	0.20
150	1.89	6.02	3.15	1.80
200	1.87	4.70	3.50	2.70

Given the exact result of the output voltage by solving the system of linear Eq. (45), the time average power can then be calculated as the total energy generated in each time interval divided by the output cycle, which can be presented as

$$P_{avg} = \frac{2}{T} \int_0^{\frac{T}{2}} \frac{\left[V_{R_L}^{(n)}(t)\right]^2}{R_L} dt \qquad (50)$$

where $T = 2\pi/\omega$ is the cycle of the excitation.

4. Validation and discussion

An electret-based microgenerator with the parameters shown in Table 2 is utilized to validate the proposed analytical model developed in Sect. 3. The device consists of two conductive plates separated by various values of air gap g as shown in Table 2. The out-of-plan length of the two plates is 10 mm. Each plate is etched and patterned with twenty 0.5-mm wide electrodes, resulting in an active overlapping area $A_0 = 100$ mm^2. A 20 µm thick electret made from Teflon PTFE with dielectric constant $\varepsilon_d = 2.1$ is corona-charged to obtain a surface potential of -100 V and attached to one plate. Sinusoidal vibrations with amplitudes equal to 1 and 1.5 mm, corresponding to $k = 2$ and $k = 3$, respectively, are applied to create relative motion between the two plates for electric power generation. The analytical results of the considered microgenerator are then calculated and compared with the numerical simulation results obtained from the finite element modeling (FEM) and numerical methods presented in (Boisseau *et al.* 2010). The lumped parasitic capacitance C_p can be determined either by measuring the intrinsic capacitance of the energy harvesting system or fitting the

numerical results of time average power. In this section, we employ the latter approach to obtain C_p as shown in Table 3. The values of the minimum and maximum capacitances, $C_{\min}$ and $C_{\max}$ used in the simulation are also summarized in Table 3.

Fig. 8 shows the calculated time-average output power generated from the microgenerator using the proposed analytical model and the numerical simulation. In general, the analytical results are in good agreements with the numerical simulation, particularly, the ability to accurately predict the effective power peak generated from the microgenerator. The discrepancy between the analytical model and numerical simulation is mainly due to the approximation made in Eq. (7). At a small value of air gap, for example $g = 100$ µm as shown in Figs. 8(a) and 8(d), the analytical model can accurately predict the output power at low values of load resistance, while notable errors can be observed at larger values of R_L. This is consistent with the assumption of small $R_L C_0$ made in Eq. (16). As the air gap increases, the stray capacitances induced by fringing fields become more significant compared to the maximum overlapping capacitances. Since the developed analytical model does include the effect of parasitic capacitances presented in Sect. 3, the analytical results at higher C_p provide a more accurate prediction of the power peaks and the optimal load resistances as shown in Figs. 8(b)-8(f). In practice, the parasitic capacitances induced by external harvesting circuitry and the microgenerator itself are often in the order to 10 pF, while the capacitances of microgenerators are only a few pF (Bartsch *et al.* 2009, Chen *et al.* 2013). The analytical model is, therefore, capable of predicting the effective power generated from practical electret-based microgenerators.

The estimated output voltage obtained for the given microgenerator is also evaluated. The results in Fig. 9 shows an adequate fit between the analytical model and the numerical simulation. The difference between the two signal shapes is, again, due to the approximation and the linearization made in Sect. 2. Another discrepancy is the sharp peaks of the output voltage at each time instance compared with the rounded curve of the numerical simulation. This mismatch is due to the non-differentiation of the theoretical overlapping area $A(t)$ at each time instance t_j in the analytical model as highlighted by the black circles shown in Fig. 10. Nevertheless, the analytical model can provide a good prediction of the output voltage with reasonable accuracy.

5. Conclusions

In summary, we successfully developed and formulated an analytical model for electret-based microgenerators under general sinusoidal excitations. Within a cycle of an excitation, the electrodynamics of a microgenerator changes from a regular to a reverse-sawtooth voltage source in series with an internal resistance or to a current source and vice versus. Parasitic capacitances are also included to refine the model for a more accurate prediction of output voltage and power.
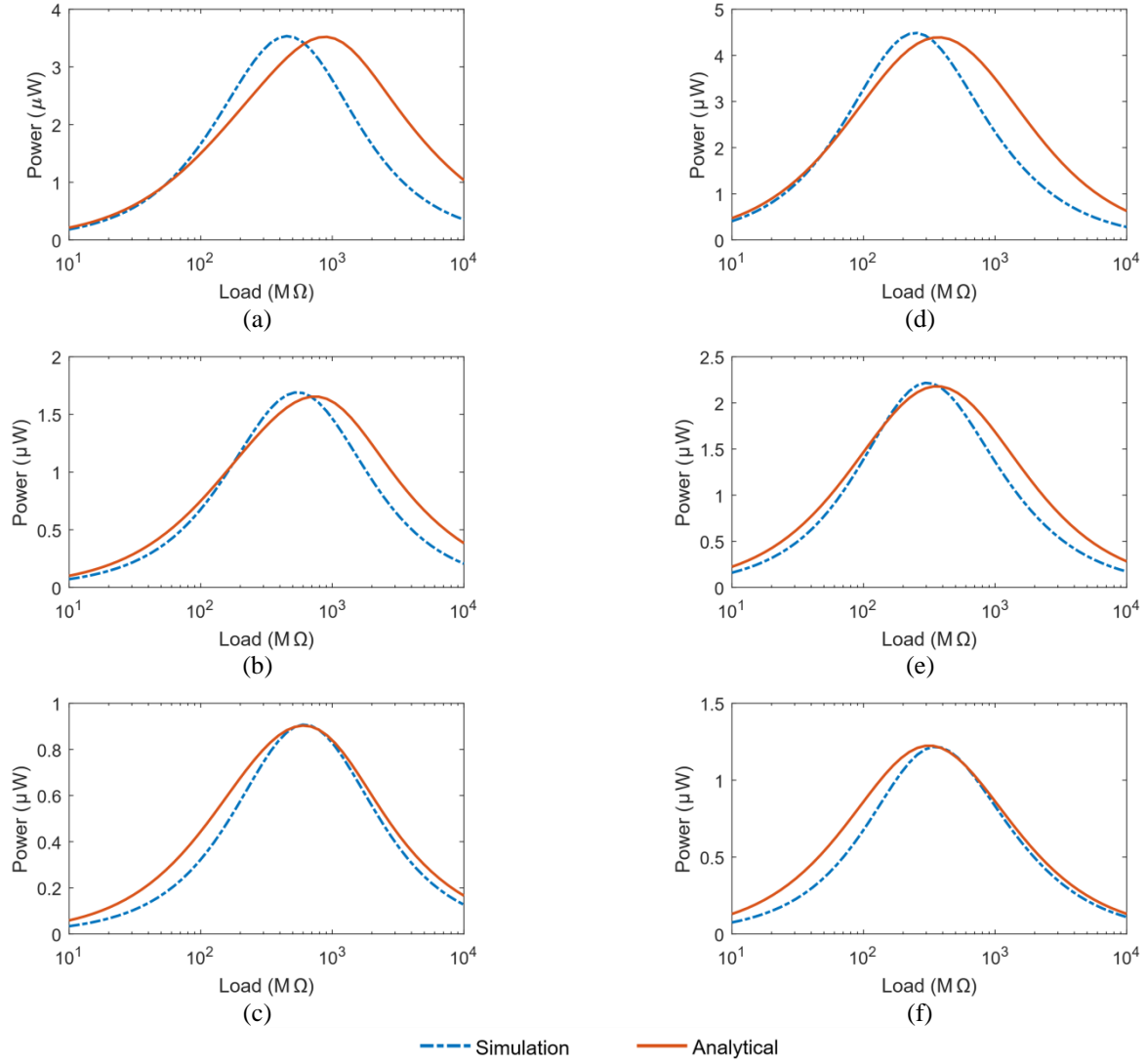
Fig. 8 Output powers generated from the microgenerator using the analytical model are in good agreement with the simulation under various excitation amplitudes and air gap distances. The left figures are for $k = 2$, while the right ones are for $k = 3$. The air gap values from top row to bottom row are respectively 100 µm, 150 µm and 200 µm
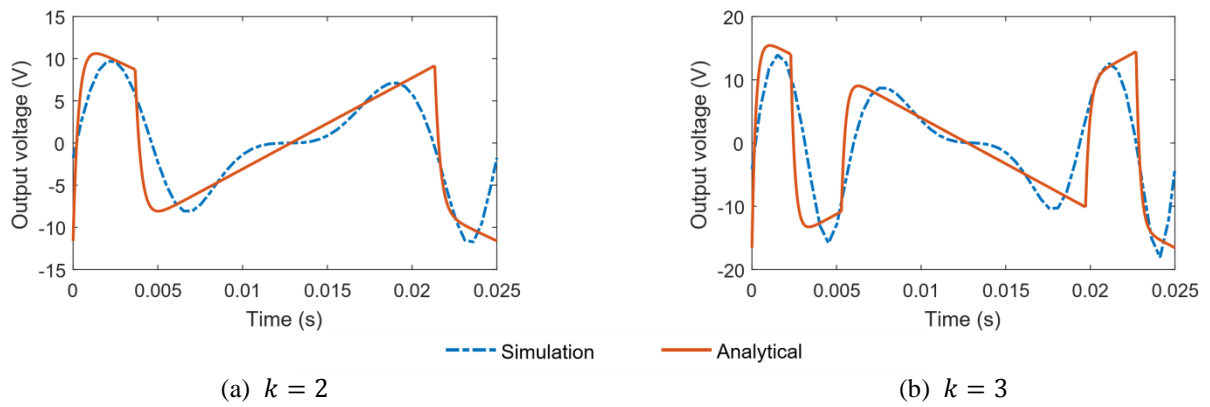

Fig. 9 The calculated output voltage using the analytical model shows an adequate fit to the numerical simulation under two different excitation amplitudes with the same load resistance $R_L = 100$ MΩ and the same air gap distance $g = 200$ µm. The discrepancy is due to the approximation from sinusoidal functions to parabolic functions and the linearization presented in Sect. 2

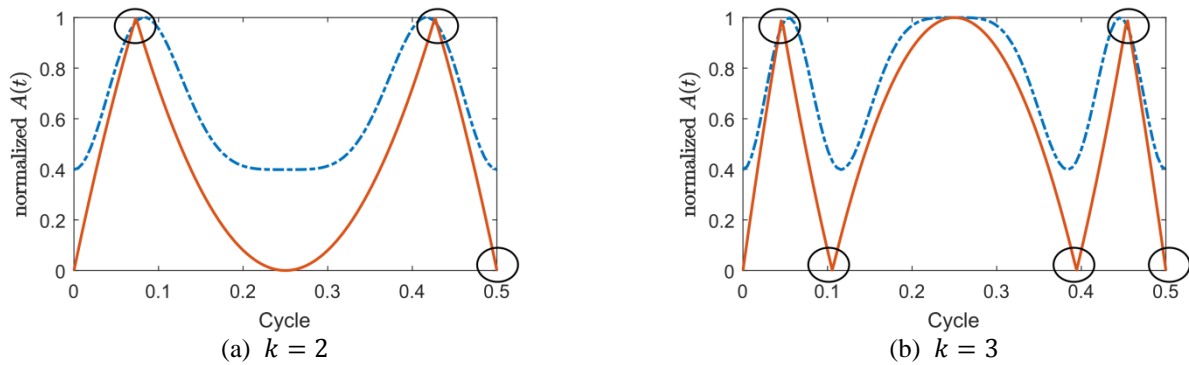(a) $k = 2$ (b) $k = 3$

Fig. 10 The non-differentiation of theoretical overlapping area highlighted in circles attributes to the discrepancy of sharp peaks in the analytical model comparing with smooth curve in the numerical simulation

The model is validated using FEM and numerical modeling's presented in the literature and shows a good agreement. Importantly, the proposed model provides an understanding and an insight into the operating mechanism of electret-based microgenerators, which is very helpful when designing and optimizing their performances.

References

Bartsch, U., Sander, C., Blattmann, M., Gaspar, J. and Paul, O. (2009), "Influence of parasitic capacitances on the power output of electret-based energy harvesting generators", *Proc. Power MEMS*, 332-335.

Bhatnagar, V. and Owende, P. (2015), "Energy harvesting for assistive and mobile applications", *Energy Sci. Eng.*, **3**(3), 153-173.

Boisseau, S., Despesse, G. and Sylvestre, A. (2010), "Optimization of an electret-based energy harvester", *Smart Mater. Struct.*, **19**(7), 75015.

Boland, J., Chao, Y.H., Suzuki, Y. and Tai, Y.C. (2003), "Micro electret power generator", *Proceedings of the 16th Annual International Conference on Micro Electro Mechanical Systems*, 2003. MEMS-03 Kyoto. IEEE.

Chen, R. and Suzuki, Y. (2013), "Suspended electrodes for reducing parasitic capacitance in electret energy harvesters", *J. Micromech. Microeng.*, **23**(12), 125015.

Franco, S. (2002), Design With Operational Amplifiers And Analog Integrated Circuits McGraw-Hill: 187-188.

Gradshteyn, I.S. and Ryzhik, I.M. (2014), Table of Integrals, Series, and Products Academic press.

Jefimenko, O.D. and Walker, D.K. (1978), "Electrostatic current generator having a disk electret as an active element", *IEEE T. Ind. Appl.*, **6**(6), 537-540.

Ju, S., Chae, S.H., Choi, Y., Lee, S., Lee, H.W. and Ji, C.H. (2013), "A low frequency vibration energy harvester using magnetoelectric laminate composite", *Smart Mater. Struct.*, **22**(11), 115037.

Kiziroglou, M.E., He, C. and Yeatman, E.M. (2009), "Rolling rod electrostatic microgenerator", *IEEE T. Ind. Electron.*, **56**(4), 1101-1108.

Lo, H.W. and Tai, Y.C. (2008), "Parylene-based electret power generators", *J. Micromech. Microeng.*, **18**(10), 104006.

Meninger, S., Mur-Miranda, J.O., Amirtharajah, R., Chandrakasan, A.P. and Lang, J.H. (2001), "Vibration-to-electric energy conversion", *IEEE T. Very Large Scale Integration Syst.*, **9**(1), 64-76.

Naruse, Y., Matsubara, N., Mabuchi, K., Izumi, M. and Suzuki, S. (2009), "Electrostatic micro power generation from low-frequency vibration such as human motion", *J. Micromech. Microeng.*, **19**(9), 94002.

Nguyen, C.C., Ranasinghe, D.C. and Al-Sarawi, S.F. (2017), "Analytical modeling and optimization of electret-based microgenerators under sinusoidal excitations", *Microsystem Technologies*, **23**(12), 5855-5865.

Perez, M., Boisseau, S., Gasnier, P., Willemin, J., Geisler, M. and Reboud, J.L. (2016), "A cm scale electret-based electrostatic wind turbine for low-speed energy harvesting applications", *Smart Mater. Struct.*, **25**(4), 45015.

Renaud, M., Altena, G., Elfrink, R., Goedbloed, M., de Nooijer, C. and van Schaijk, R. (2015), "Modeling and characterization of electret based vibration energy harvesters in slot-effect configuration", *Smart Mater. Struct.*, **24**(8), 85023.

Roundy, S. and Takahashi, E. (2013), "A planar electromagnetic energy harvesting transducer using a multi-pole magnetic plate", *Sensors Actuat. A-phys.*, **195**, 98-104.

Roundy, S. and Wright, P.K. (2004), "A piezoelectric vibration based generator for wireless electronics", *Smart Mater. Struct.*, **13**(5), 1131-1142.

Tada, Y. (1992), "Experimental characteristics of electret generator, using polymer film electrets", *Japanese J. Appl. Phys.*, **31**(3), 846-51.

Temme, N.M. (2011), Special Functions: An Introduction To The Classical Functions Of Mathematical Physics John Wiley & Sons: 110.

Torah, R., Glynne-Jones, P., Tudor, M., O'Donnell, T., Roy, S. and Beeby, S. (2008), "Self-powered autonomous wireless sensor node using vibration energy harvesting", *Meas. Sci. Technol.*, **19**(12), 125202.

Tsutsumino, T., Suzuki, Y., Kasagi, N. and Sakane, Y. (2006), "Seismic power generator using high-performance polymer electret", *Proceedings of the 19th IEEE International Conference on Micro Electro Mechanical Systems*.

Wang, H., Tang, L., Shan, X., Xie, T. and Yang, Y. (2014), "Modeling and performance evaluation of a piezoelectric energy harvester with segmented electrodes", *Smart Struct. Syst.*, **14**(2), 247-266.

Yang, Y. and Tang, L. (2009), "Equivalent circuit modeling of piezoelectric energy harvesters", *J. Intel. Mat. Syst. Str.*, **20**(18), 2223-2235.

Yang, Z., Halvorsen, E. and Dong, T. (2014), "Electrostatic energy

harvester employing conductive droplet and thin-film electret", *IEEE/ASME J. Microelectromech. Syst.*, **23**(2), 315-323.

Yen, B.C. and Lang, J.H. (2006), "A variable-capacitance vibration-to-electric energy harvester", *IEEE T. Circ. Syst.*, **53**(2), 288-295.

Yun, J., Patel, S.N., Reynolds, M.S. and Abowd, G.D. (2011), "Design and performance of an optimal inertial power harvester for human-powered devices", *IEEE T. Mobile Comput.*, **10**(5), 669-683.

HJ

Appendices

A. Integration of Eq. (12)

To employ the integrating factor to solve Eq. (12), we define a function $M_1(t)$ such that

$$
\begin{aligned}
M_1(t) &= \int \frac{dt}{4kR_LC_0\left[\frac{\omega t}{\pi}\left(1-\frac{\omega t}{\pi}\right)-\frac{m}{2k}\right]} \\
&= \frac{1}{2kR_LC_0}\int \frac{dt}{-\frac{2\omega^2}{\pi^2}t^2+\frac{2\omega}{\pi}t-\frac{m}{k}} \\
&= \frac{\pi\ln\left|\dfrac{-\frac{2\omega^2}{\pi^2}t+\frac{\omega}{\pi}-\frac{\omega}{\pi}\sqrt{1-\frac{2m}{k}}}{-\frac{2\omega^2}{\pi^2}t+\frac{\omega}{\pi}+\frac{\omega}{\pi}\sqrt{1-\frac{2m}{k}}}\right|}{4k\omega R_LC_0\sqrt{1-\frac{2m}{k}}} \\
&= \frac{\pi}{4k\omega R_LC_0\sqrt{1-\frac{2m}{k}}}\ln\left[\frac{\frac{2\omega t}{\pi}-\left(1-\sqrt{1-\frac{2m}{k}}\right)}{\left(1+\sqrt{1-\frac{2m}{k}}\right)-\frac{2\omega t}{\pi}}\right] \\
&= \gamma_{2m}\ln\left(\frac{t-t_{2m}}{t_{2k+1-2m}-t}\right)
\end{aligned}
\tag{51}
$$

where γ_j is given in Eq. (14).

The integrating factor can be calculated using the result of $M_1(t)$ and presented as

$$
e^{M_1(t)} = \left(\frac{t-t_{2m}}{t_{2k+1-2m}-t}\right)^{\gamma_{2m}}
\tag{52}
$$

The solution of Eq. (12) can, therefore, be given by

$$
\begin{aligned}
Q_1(t) &= \beta_1 e^{-M_1(t)} - \frac{V_0}{R_L}e^{-M_1(t)}\int_{t_{2m}}^{t-t_{2m}} e^{M_1(t)}dt \\
&= \beta_1\left(\frac{t_{2k+1-2m}-t}{t-t_{2m}}\right)^{\gamma_{2m}} - \frac{V_0}{R_L}\left(\frac{t_{2k+1-2m}-t}{t-t_{2m}}\right)^{\gamma_{2m}} \\
&\times \underbrace{\int_{t_{2m}}^{t-t_{2m}}\left(\frac{t-t_{2m}}{t_{2k+1-2m}-t}\right)^{\gamma_{2m}}dt}_{N_1(t)}
\end{aligned}
\tag{53}
$$

It is worthy to note that the interval of the integral given in $N_1(t)$ is chosen in this case for the time interval $[t_{2m}, t_{2m+1}]$. Similar approach can be carried out for the interval $[t_{2k-2m}, t_{2k-2m+1}]$ by replacing the time instance t_{2m} by t_{2k-2m} in the interval of the interval $N_1(t)$.

$N_1(t)$ has to be rewritten in such a form which can be calculated using the result (3.194-1) in (Gradshteyn *et al.* 2014). Let $z = t - t_{2m}$, the representation of the integral $N_1(t)$ in this case is

$$
\begin{aligned}
N_1(t) &= \int_0^z \left(\frac{z}{t_{2k+1-2m}-t_{2m}-z}\right)^{\gamma_{2m}}dz \\
&= (t_{2k+1-2m}-t_{2m})^{-\gamma_{2m}} \\
&\times \int_0^z \left(\frac{z}{1-\frac{z}{t_{2k+1-2m}-t_{2m}}}\right)^{\gamma_{2m}}dz \\
&= \frac{z^{\gamma_{2m}+1}}{(\gamma_{2m}+1)(t_{2k+1-2m}-t_{2m})^{\gamma_{2m}}} \\
&\times {}_2F_1\left(\gamma_{2m},\gamma_{2m}+1;\gamma_{2m}+2;\frac{z}{t_{2k+1-2m}-t_{2m}}\right)
\end{aligned}
\tag{54}
$$

$N_1(t)$ can be simplified by applying the Euler's transformation of hypergeometric functions (Temme 2011) to present as

$$
\begin{aligned}
N_1(t) &= \frac{z^{\gamma_{2m}+1}\left(1-\frac{z}{t_{2k+1-2m}-t_{2m}}\right)^{1-\gamma_{2m}}}{(\gamma_{2m}+1)(t_{2k+1-2m}-t_{2m})^{\gamma_{2m}}} \\
&\times {}_2F_1\left(1,2;\gamma_{2m}+2;\frac{z}{t_{2k+1-2m}-t_{2m}}\right) \\
&= \frac{(t-t_{2m})^{\gamma_{2m}+1}(t_{2k+1-2m}-t)^{1-\gamma_{2m}}}{(\gamma_{2m}+1)(t_{2k+1-2m}-t_{2m})} \\
&\times {}_2F_1\left(1,2;\gamma_{2m}+2;\frac{t-t_{2m}}{t_{2k+1-2m}-t_{2m}}\right)
\end{aligned}
\tag{55}
$$

Given the expression of $N_1(t)$, the solution $Q_1(t)$ can be expressed as

$$
\begin{aligned}
Q_1(t) &= \beta_1\left(\frac{t_{2k+1-2m}-t}{t-t_{2m}}\right)^{\gamma_{2m}} \\
&- \frac{V_0(t-t_{2m})(t_{2k+1-2m}-t)}{R_L(\gamma_{2m}+1)(t_{2k+1-2m}-t_{2m})} \\
&\times {}_2F_1\left(1,2;\gamma_{2m}+2;\frac{t-t_{2m}}{t_{2k+1-2m}-t_{2m}}\right)
\end{aligned}
\tag{13}
$$

B. Integration of Eq. (23)

A similar approach as the one presented in Appx. 0 is employed to solve Eq. (23). A function $M_{21}(t)$ is defined such that

$$
\begin{aligned}
M_{21}(t) &= \frac{1}{2kR_LC_0}\int \frac{dt}{\frac{2\omega^2}{\pi^2}t^2-\frac{2\omega}{\pi}t+\frac{m+1}{k}} \\
&= \gamma_{2m+2}\ln\left(\frac{t-t_{2k-2m-1}}{t-t_{2m+2}}\right)
\end{aligned}
\tag{56}
$$

The integrating factor is calculated using the result of the function $M_{21}(t)$ and expressed as

$$
e^{M_{21}(t)} = \left(\frac{t-t_{2k-2m-1}}{t-t_{2m+2}}\right)^{\gamma_{2m+2}}
\tag{57}
$$

The induced charge $Q_{21}(t)$ of Eq. (23) can, therefore, be written as

$$
\begin{aligned}
Q_{21}(t) &= \beta_{21}\left(\frac{t-t_{2m+2}}{t-t_{2k-2m-1}}\right)^{\gamma_{2m+2}} \\
&- \frac{V_0}{R_L}\left(\frac{t-t_{2m+2}}{t-t_{2k-2m-1}}\right)^{\gamma_{2m+2}} \\
&\times \underbrace{\int_{t_{2k-2m-1}}^{t-t_{2k-2m-1}}\left(\frac{t-t_{2k-2m-1}}{t-t_{2m+2}}\right)^{\gamma_{2m+2}}dt}_{N_{21}(t)}
\end{aligned}
\tag{58}
$$

$N_{21}(t)$ is then rewritten as

$$
\begin{aligned}
N_{21}(t) &= (t_{2k-2m-1}-t_{2m+2})^{-\gamma_{2m+2}} \\
&\times \int_0^{z_2}\left(\frac{z_2}{1+\frac{z_2}{t_{2k-2m-1}-t_{2m+2}}}\right)^{\gamma_{2m+2}}dz_2
\end{aligned}
\tag{59}
$$

where $z_2 = t - t_{2k-2m-1}$.

Applying the result (3.194-1) in (Gradshteyn *et al.* 2014) gives

$$N_{21}(t) = \frac{z_2^{\gamma_{2m+2}+1}}{(1+\gamma_{2m+2})(t_{2k-2m-1}-t_{2m+2})^{\gamma_{2m+2}}}$$
$$\times {}_2F_1\left(\gamma_{2m+2},\gamma_{2m+2}+1;\gamma_{2m+2}+2;\frac{-z_2}{t_{2k-2m-1}-t_{2m+2}}\right) \tag{60}$$

Applying Euler's transform gives

$$N_{21}(t) = \frac{(t-t_{2m+2})(t-t_{2k-2m-1})}{(1+\gamma_{2m+2})(t_{2k-2m-1}-t_{2m+2})}$$
$$\times \left(\frac{t-t_{2k-2m-1}}{t-t_{2m+2}}\right)^{\gamma_{2m+2}} \tag{61}$$
$$\times {}_2F_1\left(1,2;2+\gamma_{2m+2};\frac{t_{2k-2m-1}-t}{t_{2k-2m-1}-t_{2m+2}}\right)$$

Therefore, the solution $Q_{21}(t)$ can be obtained as

$$Q_{21}(t) = \beta_{21}\left(\frac{t-t_{2m+2}}{t-t_{2k-2m-1}}\right)^{\gamma_{2m+2}}$$
$$-\frac{V_0(t-t_{2m+2})(t-t_{2k-2m-1})}{R_L(1+\gamma_{2m+2})(t_{2k-2m-1}-t_{2m+2})} \tag{24}$$
$$\times {}_2F_1\left(1,2;2+\gamma_{2m+2};\frac{t_{2k-2m-1}-t}{t_{2k-2m-1}-t_{2m+2}}\right)$$

C. Integration of Eq. (33)

The integrating factor of equation Eq. (33) can be calculated as

$$M_{22}(t) = \int \frac{dt}{kR_LC_0\left(1-\frac{2\omega t}{\pi}\right)^2} = \frac{\pi}{2k\omega R_L C_0\left(1-\frac{2\omega t}{\pi}\right)} \tag{62}$$

Hence, the solution of Eq (33) is given by

$$Q_{22}(t) = \beta_{22}e^{\frac{-\pi}{2k\omega R_L C_0\left(1-\frac{2\omega t}{\pi}\right)}} - \frac{V_0}{R_L}e^{\frac{-\pi}{2k\omega R_L C_0\left(1-\frac{2\omega t}{\pi}\right)}}$$
$$\times \underbrace{\int e^{\frac{\pi}{2k\omega R_L C_0\left(1-\frac{2\omega t}{\pi}\right)}}dt}_{N_{22}(t)} \tag{63}$$

To obtain the solution, $N_{22}(t)$ must be determined. To achieve that, let

$$z_{22} = \frac{\pi}{2k\omega R_L C_0\left(1-\frac{2\omega t}{\pi}\right)}$$
$$\Rightarrow t = \frac{\pi}{2\omega}\left(1-\frac{\pi}{2k\omega R_L C_0 z_{22}}\right) \tag{64}$$
$$\Rightarrow dt = \frac{\pi^2}{4k\omega^2 R_L C_0 z_{22}^2}\,dz_{22}$$

$N_{22}(t)$ can be rewritten as

$$N_{22}(t) = \frac{\pi^2}{4k\omega^2 R_L C_0}\int \frac{e^{z_{22}}}{z_{22}^2}\,dz_{22} \tag{65}$$

According to the result 2.325-2 in (Gradshteyn *et al.* 2014), $N_{22}(t)$ can be expressed as

$$N_{22}(t) = \frac{\pi^2}{4k\omega^2 R_L C_0}\left[Ei(z_{22}) - \frac{e^{z_{22}}}{z_{22}}\right] \tag{66}$$

Hence, the solution $Q_{22}(t)$ of Eq. (33) can be given by

$$Q_{22}(t) = \beta_{22}e^{\frac{-\pi}{2k\omega R_L C_0\left(1-\frac{2\omega t}{\pi}\right)}} + \frac{\pi V_0}{2\omega R_L}\left(1-\frac{2\omega t}{\pi}\right)$$
$$-\frac{V_0}{R_L}\frac{\pi^2 e^{\frac{-\pi}{2k\omega R_L C_0\left(1-\frac{2\omega t}{\pi}\right)}}}{4k\omega^2 R_L C_0}$$
$$\times Ei\left[\frac{\pi}{2k\omega R_L C_0\left(1-\frac{2\omega t}{\pi}\right)}\right] \tag{34}$$